
This copy is for your personal, non-commercial use only.

If you wish to distribute this article to others, you can order high-quality copies for your colleagues, clients, or customers by [clicking here](#).

Permission to republish or repurpose articles or portions of articles can be obtained by following the guidelines [here](#).

The following resources related to this article are available online at www.sciencemag.org (this information is current as of September 29, 2014):

Updated information and services, including high-resolution figures, can be found in the online version of this article at:

<http://www.sciencemag.org/content/336/6078/202.full.html>

Supporting Online Material can be found at:

<http://www.sciencemag.org/content/suppl/2012/04/11/336.6078.202.DC1.html>

This article **cites 27 articles**, 2 of which can be accessed free:

<http://www.sciencemag.org/content/336/6078/202.full.html#ref-list-1>

This article has been **cited by** 2 articles hosted by HighWire Press; see:

<http://www.sciencemag.org/content/336/6078/202.full.html#related-urls>

This article appears in the following **subject collections**:

Physics

<http://www.sciencemag.org/cgi/collection/physics>

Demonstration of Entanglement of Electrostatically Coupled Singlet-Triplet Qubits

M. D. Shulman,^{1*} O. E. Dial,^{1*} S. P. Harvey,¹ H. Bluhm,^{1†} V. Umansky,² A. Yacoby^{1‡}

Quantum computers have the potential to solve certain problems faster than classical computers. To exploit their power, it is necessary to perform interqubit operations and generate entangled states. Spin qubits are a promising candidate for implementing a quantum processor because of their potential for scalability and miniaturization. However, their weak interactions with the environment, which lead to their long coherence times, make interqubit operations challenging. We performed a controlled two-qubit operation between singlet-triplet qubits using a dynamically decoupled sequence that maintains the two-qubit coupling while decoupling each qubit from its fluctuating environment. Using state tomography, we measured the full density matrix of the system and determined the concurrence and the fidelity of the generated state, providing proof of entanglement.

Singlet-triplet (S - T_0) qubits, a particular realization of spin qubits (*1–7*), store quantum information in the joint spin state of two electrons (*8–10*). The basis states for the S - T_0 qubit can be constructed from the eigenstates of a single electron spin, $|\uparrow\rangle$ and $|\downarrow\rangle$. We chose $|S\rangle =$

$(1/\sqrt{2})(|\uparrow\downarrow\rangle - |\downarrow\uparrow\rangle)$ and $|T_0\rangle = (1/\sqrt{2})(|\uparrow\downarrow\rangle + |\downarrow\uparrow\rangle)$ because these states are insensitive to uniform fluctuations in the magnetic field. The qubit can then be described as a two-level system with a representation on the so-called Bloch sphere (Fig. 1A). Universal quantum control is achieved using two physically distinct operations that drive rotations around the x and z axes of the Bloch sphere (*11*). Rotations around the z axis are driven by the exchange splitting, J , between $|S\rangle$ and $|T_0\rangle$, and rotations around the x axis are driven by a magnetic field gradient, ΔB_z , between the electrons.

We implemented the S - T_0 qubit by confining two electrons to a double quantum dot (QD) in a two-dimensional electron gas (2DEG) located

91 nm below the surface of a GaAs-AlGaAs heterostructure. We deposited local top gates using standard electron beam lithography techniques to locally deplete the 2DEG and form the QDs. We operated between the states $(0,2)$ and $(1,1)$, where (n_L, n_R) describes the state with $n_L(n_R)$ electrons in the left (right) QD. The $|S\rangle$ and $|T_0\rangle$ states, the logical subspace for the qubit, are isolated by applying an external magnetic field of 700 mT in the plane of the device such that the Zeeman splitting makes $T_+ = |\uparrow\uparrow\rangle$ and $T_- = |\downarrow\downarrow\rangle$ energetically inaccessible. The exchange splitting, J , is a function of the difference in energy, ϵ , between the levels of the left and right QDs. Pulsed DC electric fields rapidly change ϵ , allowing us to switch J on, which drives rotations around the z axis. When J is off, the qubit precesses around the x axis due to a fixed ΔB_z , which is stabilized to $\Delta B_z/2\pi = 30$ MHz by operating the qubit as a feedback loop between iterations of the experiment (*12*). Dephasing of the qubit rotations reflects fluctuations in the magnitude of the two control axes, J and ΔB , caused by electrical noise and variation in the magnetic field gradient, respectively. The qubit is rapidly (<50 ns) initialized in $|S\rangle$ by exchanging an electron with the nearby Fermi sea of the leads of the QD, by tuning the QD potentials so that only $|S\rangle$ lies below the Fermi energy. The qubit state is read out using standard Pauli blockade techniques, where ϵ is quickly tuned to the regime where S occupies $(0,2)$ and T_0 occupies $(1,1)$, allowing the qubit state to be determined by the proximal charge sensor. The charge state of the qubit is rapidly determined (~ 1 μ s) using standard radio frequency techniques (*13, 14*) on an adjacent sensing QD.

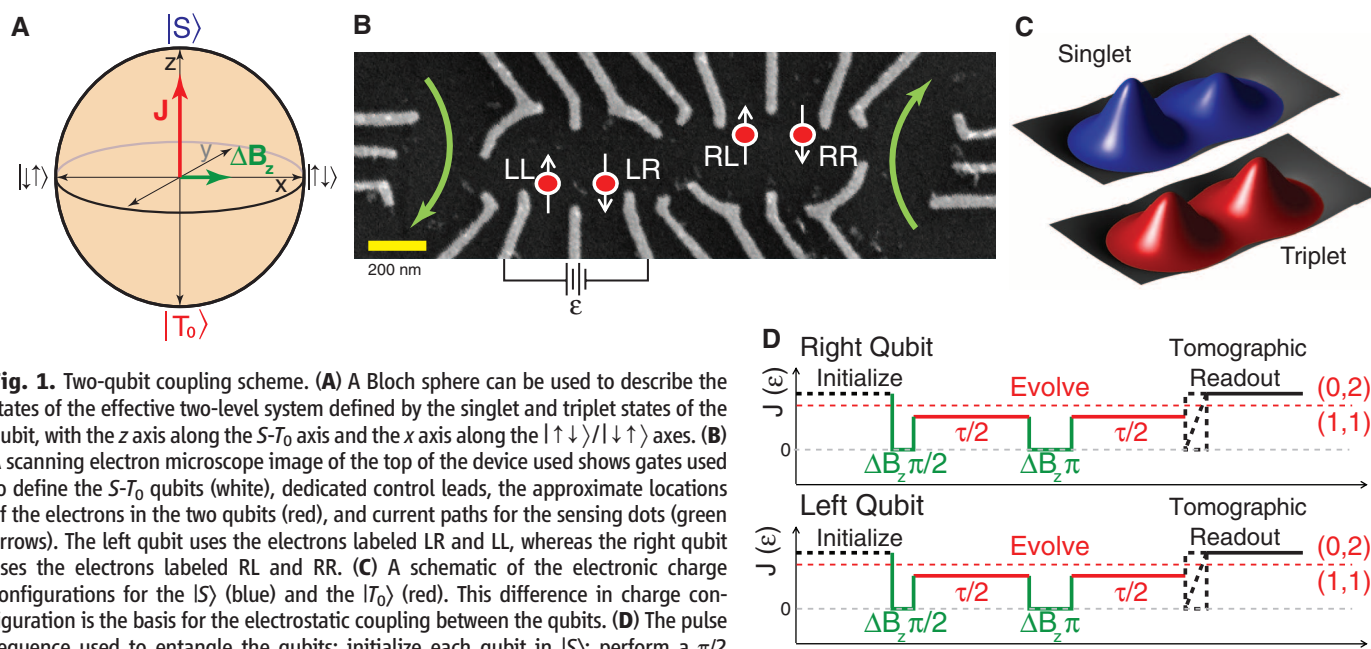


Fig. 1. Two-qubit coupling scheme. (A) A Bloch sphere can be used to describe the states of the effective two-level system defined by the singlet and triplet states of the qubit, with the z axis along the S - T_0 axis and the x axis along the $|\uparrow\downarrow\rangle/|\downarrow\uparrow\rangle$ axes. (B) A scanning electron microscope image of the top of the device used shows gates used to define the S - T_0 qubits (white), dedicated control leads, the approximate locations of the electrons in the two qubits (red), and current paths for the sensing dots (green arrows). The left qubit uses the electrons labeled LR and LL, whereas the right qubit uses the electrons labeled RL and RR. (C) A schematic of the electronic charge configurations for the $|S\rangle$ (blue) and the $|T_0\rangle$ (red). This difference in charge configuration is the basis for the electrostatic coupling between the qubits. (D) The pulse sequence used to entangle the qubits: initialize each qubit in $|S\rangle$; perform a $\pi/2$ rotation around the x axis; allow the qubits to evolve under exchange for a time $\tau/2$; perform a π rotation around the x axis, thereby decoupling the qubits from the environment but not each other; evolve under exchange for $\tau/2$; and perform state tomography to determine the resulting density matrix (fig. S3.)

To make use of the power of quantum information processing, it is necessary to perform two qubit operations in which the state of one qubit is conditioned on the state of the other (15). To investigate two-qubit operations, we fabricated two adjacent S - T_0 qubits such that they are capacitively coupled, but tunneling between them is suppressed (Fig. 1B). A charge-sensing QD next to each qubit allows for simultaneous and independent projective measurement of each qubit (see supplementary materials). We used the electrostatic coupling between the qubits to generate the two-qubit operation (16). When J is nonzero, the $|S\rangle$ and $|T_0\rangle$ states have different charge configurations in the two QDs because of the Pauli exclusion principle (Fig. 1C). This charge difference, which is a function of ϵ , causes the $|S\rangle$ and $|T_0\rangle$ states in one qubit to impose different electric fields on the other qubit. As J is a function of the electric field, the change in electric field imposed by the first qubit causes a shift in the precession frequency of the second qubit. In this way, the state of the second qubit may be conditioned on the state of the first qubit. More precisely, when a single qubit evolves under exchange, there exists a state-dependent dipole moment, \vec{d} , between $|S\rangle$ and $|T_0\rangle$, resulting from their difference in charge occupation of the QDs. Therefore, when simultaneously evolving both

qubits under exchange, they experience a capacitively mediated, dipole-dipole coupling that can generate an entangled state. The two-qubit Hamiltonian is therefore given by:

$$H_{2\text{-qubit}} = \frac{\hbar}{2} \left(J_1 (\sigma_z \otimes I) + J_2 (I \otimes \sigma_z) + \frac{J_{12}}{2} ((\sigma_z - I) \otimes (\sigma_z - I)) + \Delta B_{z,1} (\sigma_x \otimes I) + \Delta B_{z,2} (I \otimes \sigma_x) \right) \quad (1)$$

where $\sigma_{x,y,z}$ are the Pauli matrices, I is the identity operator, $\Delta B_{z,i}$, and J_i are the magnetic field gradients and the exchange splittings ($i = 1, 2$ respectively for the two qubits), and J_{12} is the two-qubit coupling, which is proportional to the product of the dipole moments in each qubit. For a two-level system with constant tunnel coupling, the dipole moment scales as $\vec{d}_i \propto \partial J_i / \partial \epsilon_i$. Empirically, we find that for experimentally relevant values of J_i , $\partial J_i / \partial \epsilon_i \propto J_i(\epsilon)$, so that $J_{12} \propto J_1 J_2$. As with the single qubit operations, this two-qubit operation requires only pulsed DC electric fields.

In principle, evolving both qubits under exchange produces an entangling gate. However, the time to produce this maximally entangled state exceeds the inhomogeneously broadened coherence times of each individual qubit, rendering

this simple implementation of the two-qubit gate ineffective. To mitigate this, we used a dynamically decoupled entangling sequence (17, 18) (Fig. 1D). In this sequence, each qubit is prepared in $|S\rangle$ and is then rotated by $\pi/2$ around the x axis ($J_i = 0$, $\Delta B_{z,i}/2\pi \approx 30$ MHz) to prepare a state in the x - y plane. The two qubits are subsequently both evolved under a large exchange splitting ($J_1/2\pi \approx 280$ MHz, $J_2/2\pi \approx 320$ MHz $\gg \Delta B_z$) for a time $\tau/2$, during which the qubits begin to entangle and disentangle. A π pulse around the x axis (ΔB_z) is then applied simultaneously to both qubits, after which the qubits are again allowed to exchange for a time $\tau/2$. This Hahn echo-like sequence (19) removes the dephasing effect of noise that is low frequency compared to $1/\tau$, and the π pulses preserve the sign of the two-qubit interaction. The resulting operation produces a controlled phase (CPhase) gate, which, in a basis of $\{|SS\rangle, |T_0S\rangle, |ST_0\rangle, |T_0T_0\rangle\}$, is an operation described by a matrix $\text{diag}(e^{-i\theta/2}, 1, 1, e^{-i\theta/2})$. For $\tau = \tau_{\text{ent}} = \frac{\pi}{(2J_{12})}$, the resulting state is a maximally entangled generalized Bell state $|\Psi_{\text{ent}}\rangle = e^{i\pi(I \otimes \sigma_y + \sigma_y \otimes I)/8} |\Psi_{-}\rangle$, which differs from the Bell state $|\Psi_{-}\rangle = (1/\sqrt{2})(|SS\rangle - |T_0T_0\rangle)$ by single-qubit rotations.

To characterize our two-qubit gate and verify that we produced an entangled state, we performed two-qubit state tomography and extracted

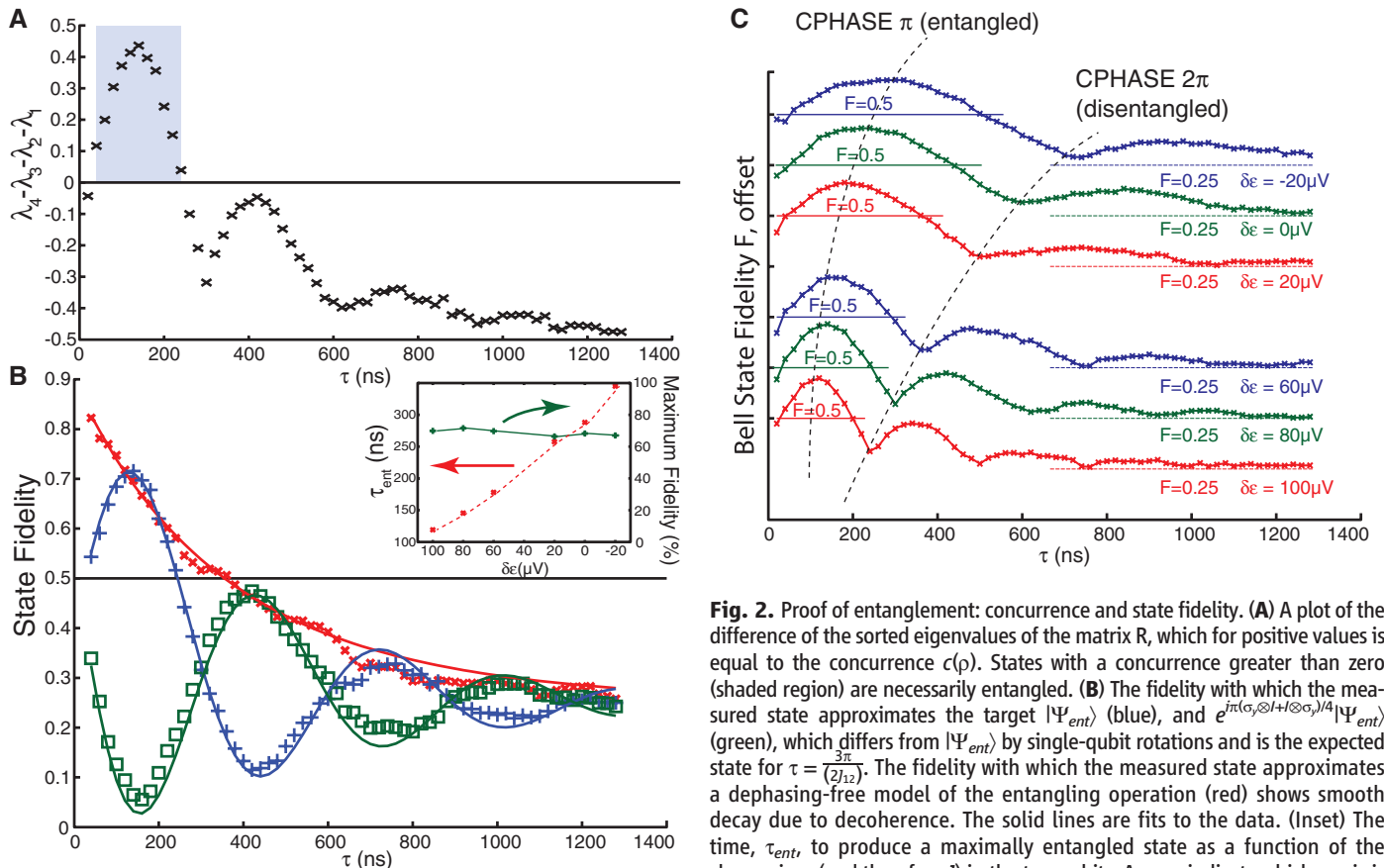


Fig. 2. Proof of entanglement: concurrence and state fidelity. **(A)** A plot of the difference of the sorted eigenvalues of the matrix R , which for positive values is equal to the concurrence $c(\rho)$. States with a concurrence greater than zero (shaded region) are necessarily entangled. **(B)** The fidelity with which the measured state approximates the target $|\Psi_{\text{ent}}\rangle$ (blue), and $e^{i\pi(\sigma_y \otimes I + I \otimes \sigma_y)/4} |\Psi_{\text{ent}}\rangle$ (green), which differs from $|\Psi_{\text{ent}}\rangle$ by single-qubit rotations and is the expected state for $\tau = \tau_{\text{ent}} = \frac{\pi}{(2J_{12})}$. The fidelity with which the measured state approximates a dephasing-free model of the entangling operation (red) shows smooth decay due to decoherence. The solid lines are fits to the data. (Inset) The time, τ_{ent} , to produce a maximally entangled state as a function of the change in ϵ (and therefore J) in the two qubits. Arrows indicate which y axis is

to be used. **(C)** The Bell state fidelity as a function of time for different values of J (offset for clarity), with guides to show where the fidelity exceeds 1/2 for each curve.

the density matrix and appropriate entanglement measures. The tomographic procedure is carefully calibrated with minimal assumptions to avoid adding spurious correlations to the data that may artificially increase the measured degree of entanglement (fig. S4). We chose the Pauli set representation of the density matrix (15, 20, 21), where we measured and plotted the 16 two-qubit correlators $\langle ij \rangle = \langle \sigma_i \sigma_j \rangle$ where σ_i are the Pauli matrices and $i, j \in \{I, X, Y, Z\}$. As a first measure of entanglement, we evaluated the concurrence (22) (Fig. 2A), $C(\rho) = \max\{0, \lambda_4 - \lambda_3 - \lambda_2 - \lambda_1\}$ for different τ , where ρ is the experimentally measured density matrix and λ_i are the eigenvalues, sorted from smallest to largest, of the matrix $R = \sqrt{\sqrt{\rho} \tilde{\rho} \sqrt{\rho}}$, and $\tilde{\rho} = (\sigma_y \otimes \sigma_y) \rho^* (\sigma_y \otimes \sigma_y)$, and ρ^* is the complex conjugate of ρ . A positive value of the concurrence is a necessary and sufficient condition for demonstration of entanglement (22). For $\tau = 140$ ns, we extracted a maximum concurrence of 0.44.

A positive value of the concurrence is a definitive proof of entanglement; however, it alone does not verify that the two-qubit operation produces the intended entangled state. To better characterize the generated quantum state, we evaluated another measure of entanglement, the Bell state fidelity, $F \equiv \langle \Psi_{ent} | \rho | \Psi_{ent} \rangle$. This may be interpreted as the probability of measuring our two-qubit state in the desired $|\Psi_{ent}\rangle$. Additionally, for all nonentangled states, one can show that $F \leq 0.5$ (23, 24). The Bell state fidelity takes the simple form $F = (1/4) \tilde{P}_{ent} \times \tilde{P}_{experiment}$, where \tilde{P}_{ent} and $\tilde{P}_{experiment}$ are the Pauli sets of a pure target Bell state and of the experimentally measured state, respectively. For our target state $|\Psi_{ent}\rangle$, the resulting Pauli set is given by $\langle XZ \rangle = \langle ZX \rangle = \langle YY \rangle = 1$, with all other elements equal to zero (Fig. 3A).

In an idealized, dephasing-free version of the experiment, as τ increases and the qubits entangle and disentangle, we expect the nonzero elements of the Pauli set for the resulting state to be

$$\begin{aligned} \langle YI \rangle &= \langle IY \rangle = \cos(J_{12}\tau), \\ \langle XZ \rangle &= \langle ZX \rangle = \sin(J_{12}\tau), \langle YY \rangle = 1 \end{aligned} \quad (2)$$

Dephasing due to electrical noise causes the amplitudes of the Pauli set to decay. However, the two-qubit Hamiltonian (Eq. 1) includes rapid single-qubit rotations around the $S-T_0$ axis ($J_1, J_2 \gg J_{12}/2\pi \approx 1$ MHz) that change with τ because of imperfect pulse rise times in the experiment. These contribute additional single-qubit rotations around the $S-T_0$ axis of each qubit, not accounted for in Eq. 2. We determined the angle of the single-qubit rotations by performing a least-squares analysis to find the single-qubit rotations that map the experimental data to the expected state without rotations (eq. S1), which is a modified form of Eq. 2 that accounts for dephasing. The decays due to dephasing were fit by calculating $\rho(t)$ in the presence of noise on J_1 and J_2 , which leads to decay of certain terms in the density matrix (25, 26). For the present case, where $J_{12} \ll J_1, J_2$, we neglected the two-qubit de-

phasing, which is smaller than single-qubit dephasings by a factor of $J_1/J_{12}, J_2/J_{12} \approx 300$, and we extracted a separate dephasing time for each individual qubit. We removed the single-qubit rotations numerically to simplify the presentation of the data (Fig. 3E). The extracted angles exhibit a smooth monotonic behavior that is consistent with their underlying origin (fig. S5).

In the absence of dephasing, we would expect the Bell state fidelity to oscillate between 0.5 for an unentangled state and 1 for an entangled state as a function of τ . This oscillation is caused by the phase accumulated by a CPhase gate between the two qubits. However, the qubits dephase as the state becomes increasingly mixed, and the amplitude of the oscillation decays to 0.25. Indeed, the following behavior is observed (Fig. 2B): For very short τ , there is very little dephasing present, and the qubits are not entangled. As τ increases, the Bell state fidelity increases as the qubits entangle, reaching a maximum value of 0.72 at $\tau = 140$ ns. As τ is increased further, we

continue to see oscillations in the Bell state fidelity, but because of dephasing, they do not again rise above 0.5.

Figure 2C shows these oscillations in Bell state fidelity as a function of τ for several different values of J as ε is changed symmetrically in the two qubits. We see that as the value of J increases in the two qubits, the time required to produce a maximally entangled state, τ_{ent} , decreases, but the maximum attainable fidelity is approximately constant. This is consistent with the theory that $J_{12} \propto \partial J_1 / \partial \varepsilon_1 \cdot \partial J_2 / \partial \varepsilon_2 \propto J_1 \cdot J_2$.

To further understand the evolution of the quantum state, we focused on one value of J and compared the measured Pauli set to that expected from single-qubit dephasing rates and J_{12} (eq. S1). Figure 3A shows the Pauli set for the measured and expected quantum states for $\tau = 40$ ns, which shows three large bars in the $\langle YI \rangle$, $\langle IY \rangle$, and $\langle YY \rangle$ components of the Pauli set. This is a nearly unentangled state. At $\tau = 140$ ns, we see weight in the $\langle XZ \rangle$, $\langle ZX \rangle$, and $\langle YY \rangle$ components of the Pauli

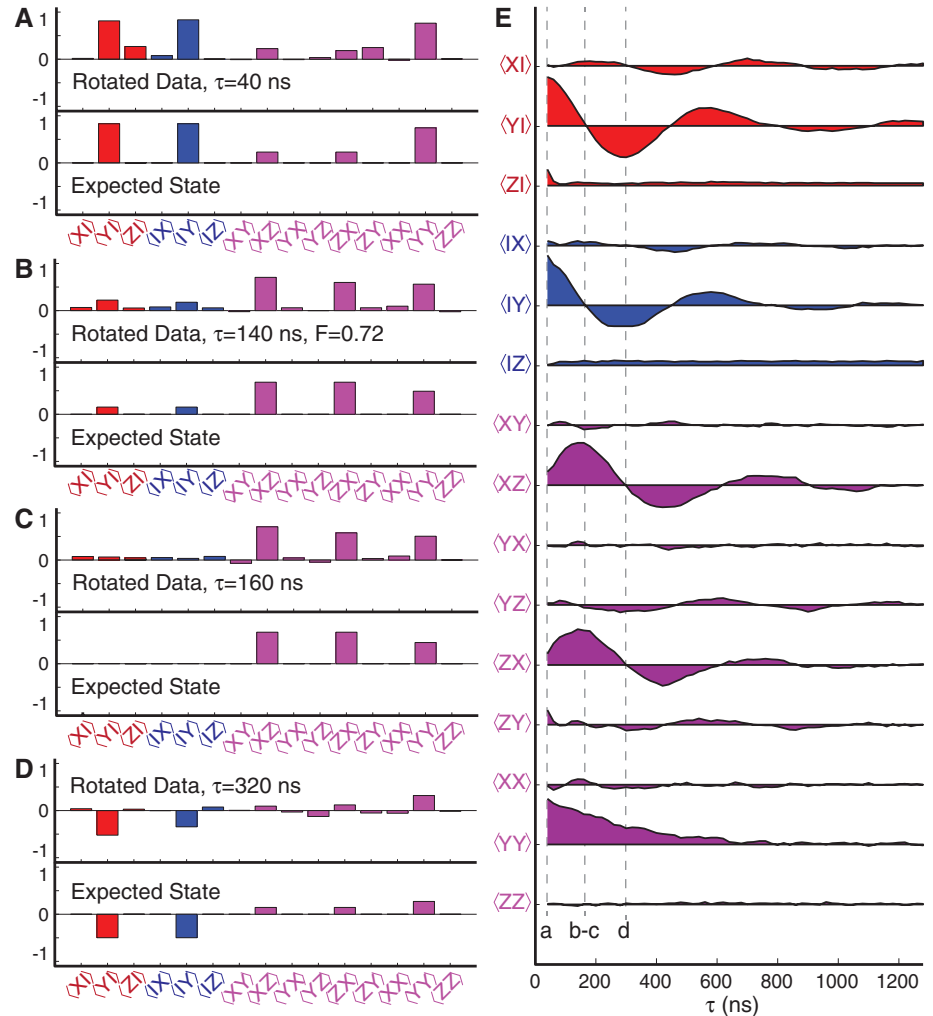


Fig. 3. Pauli set representation. (A) The elements of the Pauli set for the measured density matrix and the state expected from the entangling and dephasing rates for small τ (unentangled). The Pauli set of the measured and expected states for (B) $\tau = 140$ ns (maximum Bell state fidelity 0.72); (C) $\tau = \tau_{ent} = 160$ ns, which is a CPhase of π ; and (D) $\tau = 320$ ns, which is an unentangled state. (E) The full measured Pauli set as a function of τ , which shows the expected behavior for a gate. The y axes of adjacent elements in the Pauli set are offset by 1.

set (Fig. 3B), and we extracted a Bell state fidelity of 0.72, which demonstrates the production of an entangled state. For $\tau = \tau_{\text{ent}} = \frac{\pi}{(2J_{12})} = 160$ ns (Fig. 3C), we see a similar state to $\tau = 140$ ns, but with less weight in the single-qubit components of the Pauli set. This state corresponds to the intended CPhase of π , although the fidelity is slightly lower than at $\tau = 140$ ns due to additional decoherence. Finally, at $\tau = \pi/J_{12} = 320$ ns (Fig. 3D), where we expect the state to be unentangled, we again see large weight in the $\langle YI \rangle$, $\langle IY \rangle$, and $\langle YY \rangle$ components of the Pauli set, although the bars are shorter than the Pauli set for $\tau = 40$ ns because of dephasing of the qubits. We plotted the entire Pauli set as a function of time (Fig. 3E), which clearly shows the predicted oscillation (Eq. 2) between $\langle YI \rangle, \langle IY \rangle$ and $\langle XZ \rangle, \langle ZX \rangle$, with decays due to decoherence.

The two-qubit gate that we have demonstrated is an important step toward establishing a scalable architecture for quantum information processing in $S-T_0$ qubits. Although a Bell state fidelity of 0.72 is not as high as what has been reported in other solid state implementations of qubits (21, 27), there are easily implemented improvements to this two-qubit gate. State fidelity is lost to dephasing from electrical noise, and decreasing the ratio $\tau_{\text{ent}}/T_2^{\text{echo}}$, where T_2^{echo} is the single-qubit coherence time with an echo pulse, is therefore paramount to generating high-fidelity Bell states. Large improvements can be made by introducing an electrostatic coupler between the two qubits (28) to increase the two-qubit cou-

pling (J_{12}) and reduce τ_{ent} . We estimate that in the absence of other losses, if an electrostatic coupler were used, a Bell state with fidelity exceeding 90% could be produced. Other improvements can be made by studying the origins and properties of the charge noise that dephases the qubit and mitigating its adverse effects in order to increase T_2^{echo} . This would allow future tests of complex quantum operations, including quantum algorithms and quantum error correction. Finally, the addition of electrostatic couplers would allow the qubits to be spatially separated and is a path toward implementing surface codes for quantum computation.

References and Notes

1. D. Loss, D. P. DiVincenzo, *Phys. Rev. A* **57**, 120 (1998).
2. F. H. L. Koppens *et al.*, *Nature* **442**, 766 (2006).
3. M. Pioro-Ladriere *et al.*, *Nat. Phys.* **4**, 776 (2008).
4. K. C. Nowack, F. H. L. Koppens, Y. V. Nazarov, L. M. K. Vandersypen, *Science* **318**, 1430 (2007).
5. M. Pioro-Ladriere, Y. Tokura, T. Kubo, S. Tarucha, *Appl. Phys. Lett.* **90**, 024105 (2007).
6. H. O. H. Churchill *et al.*, *Phys. Rev. Lett.* **102**, 166802 (2009).
7. S. Nadj-Perge, S. M. Frolov, E. P. Bakkers, L. P. Kouwenhoven, *Nature* **468**, 1084 (2010).
8. J. Levy, *Phys. Rev. Lett.* **89**, 147902 (2002).
9. J. R. Petta *et al.*, *Science* **309**, 2180 (2005).
10. J. M. Taylor *et al.*, *Phys. Rev. B* **76**, 035315 (2007).
11. S. Foletti, H. Bluhm, D. Mahalu, V. Umansky, A. Yacoby, *Nat. Phys.* **5**, 903 (2009).
12. H. Bluhm, S. Foletti, D. Mahalu, V. Umansky, A. Yacoby, *Phys. Rev. Lett.* **105**, 216803 (2010).
13. D. J. Reilly, C. M. Marcus, M. P. Hanson, A. C. Gossard, *Appl. Phys. Lett.* **91**, 162101 (2007).
14. C. Barthel, D. J. Reilly, C. M. Marcus, M. P. Hanson, A. C. Gossard, *Phys. Rev. Lett.* **103**, 160503 (2009).

15. M. A. Nielsen, I. L. Chuang, *Quantum Computation and Quantum Information* (Cambridge Univ. Press, Cambridge, 2000).
16. J. M. Taylor *et al.*, *Nat. Phys.* **1**, 177 (2005).
17. L. Viola, E. Knill, S. Lloyd, *Phys. Rev. Lett.* **82**, 2417 (1999).
18. D. Leibfried *et al.*, *Nature* **422**, 412 (2003).
19. E. L. Hahn, *Phys. Rev.* **80**, 580 (1950).
20. F. V. Daniel, *Phys. Rev. A* **64**, 052312 (2001).
21. J. M. Chow *et al.*, *Phys. Rev. A* **81**, 062325 (2010).
22. S. Hill, W. Wootters, *Phys. Rev. Lett.* **78**, 5022 (1997).
23. C. A. Sackett *et al.*, *Nature* **404**, 256 (2000).
24. C. H. Bennett *et al.*, *Phys. Rev. Lett.* **76**, 722 (1996).
25. T. Yu, J. H. Eberly, *Opt. Commun.* **264**, 393 (2006).
26. L. Cywinski, R. M. Lutchyn, C. P. Nave, S. Das Sarma, *Phys. Rev. B* **77**, 174509 (2008).
27. M. Ansmann *et al.*, *Nature* **461**, 504 (2009).
28. L. Trifunovic *et al.*, *Phys. Rev. X* **2**, 011006 (2012).

Acknowledgments: This work is supported through the U.S. Army Research Office (ARO) Precision Quantum Control and Error-Suppressing Quantum Firmware for Robust Quantum Computing and the Intelligence Advanced Research Projects Activity (IARPA) Multi-Qubit Coherent Operations (MQCO) Program. This work was partially supported by the ARO under contract W911NF-11-1-0068. This work was performed in part at the Center for Nanoscale Systems (CNS), a member of the National Nanotechnology Infrastructure Network (NNIN), which is supported by the National Science Foundation under NSF award ECS-0335765. CNS is part of Harvard University. V.U. prepared the crystal; M.D.S. fabricated the sample; and M.D.S., O.E.D., H.B., S.P.H., and A.Y. carried out the experiment, analyzed the data, and wrote the paper. The authors declare no competing financial interests.

Supplementary Materials

www.sciencemag.org/cgi/content/full/336/6078/202/DC1
Materials and Methods
Figs. S1 to S5
References

9 December 2011; accepted 7 March 2012
10.1126/science.1217692

Topological Transitions in Metamaterials

Harish N. S. Krishnamoorthy,^{1,2*} Zubin Jacob,^{3*} Evgenii Narimanov,⁴
Ilona Kretzschmar,⁵ Vinod M. Menon^{1,2†}

Light-matter interactions can be controlled by manipulating the photonic environment. We uncovered an optical topological transition in strongly anisotropic metamaterials that results in a dramatic increase in the photon density of states—an effect that can be used to engineer this interaction. We describe a transition in the topology of the iso-frequency surface from a closed ellipsoid to an open hyperboloid by use of artificially nanostructured metamaterials. We show that this topological transition manifests itself in increased rates of spontaneous emission of emitters positioned near the metamaterial. Altering the topology of the iso-frequency surface by using metamaterials provides a fundamentally new route to manipulating light-matter interactions.

Metamaterials are artificial media in which the subwavelength features of the designed unit cells and coupling between them governs the macroscopic electro-

magnetic properties (1). This control over material parameters has led to new applications (2–4) and also the ability to mimic and study physical processes, which is difficult by other methods (5–7). One specific design freedom afforded by metamaterials is the control over the iso-frequency surface, the surface of allowed wavevectors at constant frequency (8, 9). The topology of this surface governs wave dynamics inside a medium.

The ideas of mathematical topology play an important role in many aspects of modern physics, from phase transitions to field theory to nonlinear dynamics (10, 11). An important example of this is the Lifshitz transition (12), in which the transformation of the Fermi surface of a metal

from a closed to an open geometry (because of, for example, external pressure) leads to a dramatic effect on the electron magneto-transport (13). In optics, the role of the Fermi surface is played by the optical iso-frequency surface $\omega(\vec{k}) = \text{const}$, which can be engineered by tailoring the dielectric tensor, $\vec{\epsilon}(\vec{r})$. We use this to demonstrate the optical equivalent of the “Lifshitz transition”—the optical topological transition (OTT) in which the very nature of the electromagnetic radiation in the metamaterial undergoes a drastic change. Effects on the kinetic and thermodynamic properties, such as the dynamics of propagating waves supported by the system and the electromagnetic energy density, respectively, are modified at the transition point and can be probed by following the light-metamaterial interaction using a quantum emitter.

We considered a metamaterial structure that has a uniaxial form of the dielectric tensor $\vec{\epsilon}(\vec{r}) = \text{diag}(\epsilon_{xx}, \epsilon_{yy}, \epsilon_{zz})$, where $\epsilon_{xx} = \epsilon_{yy} = \epsilon_{\parallel}$ and $\epsilon_{zz} = \epsilon_{\perp}$. The iso-frequency surface for the extraordinary (TM-polarized) waves propagating in such a strongly anisotropic metamaterial is given by

$$\frac{k_x^2 + k_y^2}{\epsilon_{\perp}} + \frac{k_z^2}{\epsilon_{\parallel}} = \frac{\omega^2}{c^2} \quad (1)$$

Closed iso-frequency surfaces differing from a simple sphere (such as an ellipsoid) can occur in these metamaterials when $\epsilon_{\parallel}, \epsilon_{\perp} > 0$ and

¹Department of Physics, Queens College, City University of New York (CUNY) and Center for Photonic and Multiscale Nanomaterials, Flushing, NY 11367, USA. ²Department of Physics, Graduate Center, CUNY, New York, NY 10016, USA. ³Department of Electrical and Computer Engineering, University of Alberta, Edmonton T6G 2V4, Canada. ⁴Birk Nanotechnology Center, School of Electrical and Computer Engineering, Purdue University, West Lafayette, IN 47907, USA. ⁵Department of Chemical Engineering, City College, CUNY, New York, NY 10031, USA.

*These authors contributed equally to this work.

†To whom correspondence should be addressed. E-mail: vmenon@qc.cuny.edu